Available online at www.sciencedirect.com
ScienceDirect
Journal of Nuclear Materials 367–370 (2007) 305–310
journal of nuclear materials
www.elsevier.com/locate/jnucmat

Diffraction imaging and diffuse scattering by small dislocation loops

Z. Zhou [a], S.L. Dudarev [b,c,*], M.L. Jenkins [a], A.P. Sutton [c], M.A. Kirk [d]

[a] Department of Materials, University of Oxford, Parks Road, Oxford OX1 3PH, UK
[b] EURATOM/UKAEA Fusion Association, Culham Science Centre, Oxfordshire OX14 3DB, UK
[c] Department of Physics, Imperial College, Exhibition Road, London SW7 2AZ, UK
[d] Materials Science Division, Argonne National Laboratory, Argonne, IL 60439, USA

Abstract

Defining the limits of visibility of small defect clusters and dislocation loops, and optimal diffraction conditions for electron microscope imaging remains one of the central problems of electron microscopy of irradiated materials. Using computer image simulations based on the propagation–interpolation algorithm for solving the Howie–Basinski equations, we investigate the relation between the actual and the 'observed' size of small loops, the part played by many-beam dynamical diffraction effects, and limitations of electron microscope imaging in identifying the structure of small defects. We also discuss the link between real-space imaging and diffuse scattering by small dislocation loops.

1. Introduction

Electron microscopy of irradiated materials is arguably the only available method of visualizing defect structures formed under irradiation. For example, small dislocation loops and point-defect clusters in crystals are usually investigated using diffraction contrast images produced by transmission electron microscopy. For relatively large defects a combination of dynamical imaging and image contrast simulations has proven very successful for determining defect structures [1]. At the same time very small clusters are usually better seen under weak-beam diffraction conditions. Image simulations are necessary for a full analysis of such images [2,3].

In this paper we give a brief review of a recently developed propagation–interpolation algorithm for solving the Howie–Basinski equations [4] and its applications to simulating electron microscope images of small dislocation loops. We also outline the principles of observation of electron diffuse scattering by *individual* defects [6].

2. The propagation–interpolation algorithm

In many-beam dynamical diffraction theory the wave function $\psi(\mathbf{r}) = \psi(x, y, z)$ of high-energy electrons propagating through a thin foil is approximated by a sum of plane waves with slowly varying amplitudes $\phi_{\mathbf{g}}(\mathbf{r})$ as

* Corresponding author. Address: EURATOM/UKAEA Fusion Association, Culham Science Centre, Oxfordshire OX14 3DB, UK. Tel.: +44 1235 466 513; fax: +44 1235 466 435.
E-mail address: sergei.dudarev@ukaea.org.uk (S.L. Dudarev).

0022-3115/$ - see front matter © 2007 Elsevier B.V. All rights reserved.
doi:10.1016/j.jnucmat.2007.03.135

$$\psi(\mathbf{r}) = \sum_{\mathbf{g}} \phi_{\mathbf{g}}(\mathbf{r}) \exp[2\pi i(\mathbf{k} + \mathbf{g} + \mathbf{s}_{\mathbf{g}}) \cdot \mathbf{r}]. \quad (1)$$

Here $\mathbf{k}$ is the wave vector of electrons incident on the foil and $\mathbf{s}_{\mathbf{g}}$ is the excitation error for the beam with diffraction vector $\mathbf{g}$. Vector $\mathbf{s}_{\mathbf{g}}$ is parallel to the zone axis $\mathbf{z}$ and its length is defined by the condition of energy conservation $\mathbf{k}^2 = |\mathbf{k} + \mathbf{g} + \mathbf{s}_{\mathbf{g}}|^2$. The potential of interaction between the high-energy electrons and the crystal is evaluated using the deformable ion approximation

$$V(\mathbf{r}) = \sum_{\mathbf{g}} V_{\mathbf{g}} \exp[2\pi i \mathbf{g} \cdot (\mathbf{r} - \mathbf{R}(\mathbf{r}))], \quad (2)$$

where $\mathbf{R}(\mathbf{r})$ is the field of atomic displacements around a defect. In our simulations this field is assumed to be continuous and is evaluated either by using linear anisotropic elasticity [5] or by interpolating between discrete atomic positions found using molecular statics or molecular dynamics.

By inserting (1) and (2) into the Schrödinger equation and neglecting the second order derivatives, we arrive at the Howie–Basinski equations [4]

$$\begin{aligned}(\mathbf{k} + \mathbf{g} + \mathbf{s}_{\mathbf{g}}) \cdot \nabla \phi_{\mathbf{g}} = {} & -i\pi U_0 \phi_{\mathbf{g}} - i\pi \sum_{\mathbf{g}'} (1 - \delta_{\mathbf{g}\mathbf{g}'}) \\ & \times U_{\mathbf{g}-\mathbf{g}'} \exp[2\pi i(\mathbf{g}' - \mathbf{g})\mathbf{R}(\mathbf{r}) \\ & + 2\pi i(\mathbf{s}_{\mathbf{g}'} - \mathbf{s}_{\mathbf{g}}) \cdot \mathbf{r}] \phi_{\mathbf{g}'}, \end{aligned} \quad (3)$$

where $U_{\mathbf{g}} = -(2m/h^2)V_{\mathbf{g}}$ and $h = 2\pi\hbar$ is the Planck constant. To eliminate the phase factors in Eq. (3) we apply a gauge transformation

$$\phi_{\mathbf{g}}(\mathbf{r}) = \Phi_{\mathbf{g}}(\mathbf{r}) e^{-2\pi i \mathbf{g} \cdot \mathbf{R}(\mathbf{r})} e^{-2\pi i \mathbf{s}_{\mathbf{g}} \cdot \mathbf{r}} e^{-i\pi \frac{U_0}{(\mathbf{k}+\mathbf{g}+\mathbf{s}_{\mathbf{g}})_z} z}. \quad (4)$$

The new amplitudes $\Phi_{\mathbf{g}}(\mathbf{r})$ satisfy equations

$$\begin{aligned}(\mathbf{k} + \mathbf{g} + \mathbf{s}_{\mathbf{g}}) \cdot \nabla \Phi_{\mathbf{g}} = {} & 2\pi i(\mathbf{k} + \mathbf{g} + \mathbf{s}_{\mathbf{g}}) \cdot \mathbf{s}_{\mathbf{g}}^{(\mathbf{R})} \Phi_{\mathbf{g}} \\ & - \pi i \sum_{\mathbf{g}'} (1 - \delta_{\mathbf{g}\mathbf{g}'}) U_{\mathbf{g}-\mathbf{g}'} \Phi_{\mathbf{g}'}, \end{aligned} \quad (5)$$

where $\mathbf{s}_{\mathbf{g}}^{(\mathbf{R})} = \mathbf{s}_{\mathbf{g}} + \nabla[\mathbf{g} \cdot \mathbf{R}(\mathbf{r})]$ is an effective excitation error that varies spatially as a function of the distortion field $\partial R_i/\partial x_j$, where $i,j = 1,2,3$. Since $\phi_{\mathbf{g}}$ and $\Phi_{\mathbf{g}}$ in Eq. (4) differ only by a phase factor, the gauge transformation does not affect the intensities of the transmitted and diffracted beams and the simulated images. The lattice distortion introduced by a defect appears only in the local excitation error $\mathbf{s}_{\mathbf{g}}^{(\mathbf{R})}$. If the crystal undergoes a homogeneous (affine) transformation then $\mathbf{s}_{\mathbf{g}}^{(\mathbf{R})}$ is a constant, and Eq. (5) describes the diffraction from a homogeneously deformed crystal. This suggests that Eq. (5) may be solved numerically for an arbitrarily deformed crystal by dividing it into small cells and taking $\mathbf{s}_{\mathbf{g}}^{(\mathbf{R})}$ as a constant within each cell. Anomalous absorption is introduced phenomenologically by adding an imaginary part to the Fourier components of the potential [7,8].

If the column approximation is applied to the transformed equations (5) we neglect the components of $\nabla\Phi_{\mathbf{g}}$ perpendicular to the zone axis $\mathbf{z}$. In this case we arrive at the *modified* Howie–Whelan equations

$$\begin{aligned}\frac{\partial \Phi_{\mathbf{g}}}{\partial z} = {} & \frac{2\pi i}{\beta_{\mathbf{g}}} (\mathbf{k} + \mathbf{g} + \mathbf{s}_{\mathbf{g}}) \cdot \mathbf{s}_{\mathbf{g}}^{(\mathbf{R})} \Phi_{\mathbf{g}} \\ & - \pi i \sum_{\mathbf{g}'} (1 - \delta_{\mathbf{g}\mathbf{g}'}) \frac{U_{\mathbf{g}-\mathbf{g}'}}{\beta_{\mathbf{g}}} \Phi_{\mathbf{g}'}, \end{aligned} \quad (6)$$

where $\beta_{\mathbf{g}} = (\mathbf{k} + \mathbf{g} + \mathbf{s}_{\mathbf{g}})_z$.

In principle, solving Eq. (5) numerically requires integrating these equations along the characteristics defined by the directions of propagation of diffraction beams $\mathbf{k} + \mathbf{g} + \mathbf{s}_{\mathbf{g}}$. The algorithm developed here replaces propagating solutions along the characteristics by a sequence of two-step events, where the first step involves solving the modified Howie–Whelan equations (6) for a thin slice within a set of adjacent narrow columns, and the second step corrects the solution for the effect of inclined propagation of the beams by means of interpolating between values found at the first step for the adjacent columns. It can be proven [10] that in the limit of small slice thickness and small column width a solution found using the propagation–interpolation algorithm is equivalent to the solution found by integrating the Howie–Basinski equations.

What are the advantages of the approach described above over the existing methods of image simulations [9,3]? On the one hand, the new algorithm makes it possible to simulate images of three-dimensional defect structures (see, e.g. [2]) while the earlier solutions of the Howie–Basinski equations only addressed the case of infinite straight dislocations [9]. In comparison with the multislice algorithms [3] the method is more flexible and is able to use as input the distortion field $\partial R_i/\partial x_j$ evaluated using either linear elasticity or atomistic simulations. Also, the structure of Eq. (5) makes it possible to select, at the start of a simulation, a set of $\mathbf{g}$-vectors that contribute to the formation of the image, therefore avoiding using a large number of virtual reflections required for carrying out a multislice simulation. Last but not least, the simplicity of the propagation–interpolation algorithm

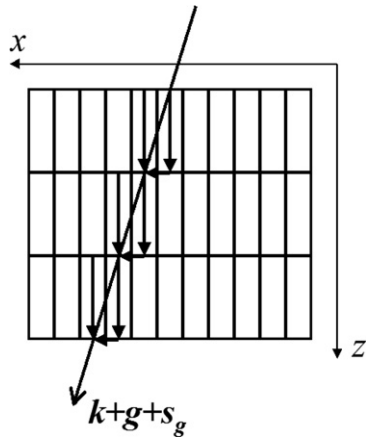

Fig. 1. Sketch illustrating the numerical implementation of the propagation–interpolation algorithm. Integrating the Howie–Basinski equations along a characteristic is replaced by a two-step process involving integrating the modified Howie–Whelan equations for two neighbouring columns and evaluating a weighted average of the two solutions.

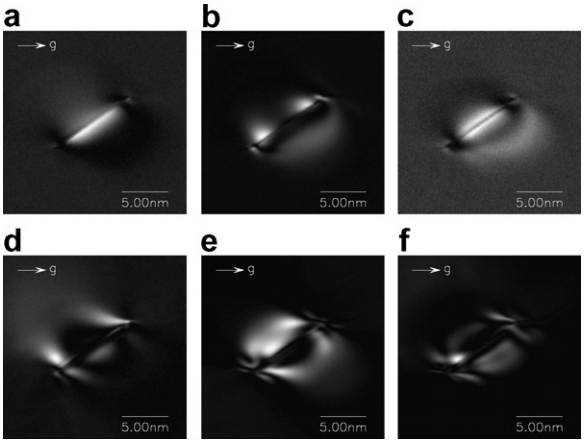

Fig. 2. Simulated weak-beam images of an edge-on dislocation loop of diameter 10 nm with Burgers vector $\mathbf{b} = 1/3[1\bar{1}1]$ at the centre of the foil of thickness 60 nm under various diffraction conditions $(\mathbf{g}, n\mathbf{g})$ for $\mathbf{g} = 002$. (a) $n = 3.5$, (b) $n = 4.5$, (c) $n = 5.5$, (d) $n = 4.0$, (e) $n = 5.0$ and (f) $n = 6.0$.

illustrated in Fig. 1 greatly assisted the numerical implementation of the method and made it possible to perform simulations of images for a large variety of diffraction conditions [10,2].

3. Image simulations

To illustrate a range of applications of the method we carried out a study of images of small Frank loops in copper simulated under weak-beam diffraction conditions. This choice was motivated by the availability of experimental images taken under well-controlled diffraction conditions of small point-defect clusters in ion-irradiated copper [11]. The parameters considered included the foil thickness and defect depth, which are difficult to determine experimentally, as well as the weak-beam imaging condition defined by the deviation parameter $|\mathbf{s}_\mathbf{g}|$ or, equivalently, by the value of parameter n entering the definition of the weak-beam condition $(\mathbf{g}, n\mathbf{g})$. The simulations were performed for Frank loops of various size and orientation. A more comprehensive description of the method and simulations is given in Ref. [10]. Our simulations show that the contrast of images depends on the position of the loop in the foil, on the thickness of the foil and on the weak-beam parameter n. At a foil thickness corresponding to a thickness fringe minimum the contrast of images is high, while at a thickness fringe maximum the contrast is relatively weak, making small loops effectively invisible [10].

To investigate the part played by many-beam diffraction effects we simulated images of small loops for varying diffraction conditions. Results of the simulations are shown in Fig. 2. The images forming the top row (images (a)–(c)) correspond to cases where n is non-integer and where no higher-order systematic reflections are excited. Simulated images shown in the bottom line (d)–(f) correspond to cases where reflections $4\mathbf{g}$, $5\mathbf{g}$ and $6\mathbf{g}$, respectively, are at the exact Bragg condition. The presence of the additional excited diffraction beams gives rise to the fairly complex pattern of intensity distribution seen in the images. Whilst it is still possible to identify the dislocation loop in the image, we see that it is desirable to avoid exciting systematic reflections simultaneously in practical weak-beam imaging. In other words, while the $(\mathbf{g}, n\mathbf{g})$ weak-beam images with integer n are known to produce artifacts in the case of line dislocations, our simulations show that artifacts also occur in the images of small loops.

One of the objectives of electron microscope examination of an irradiated specimen is establishing a reliable link between the *visible* size of a small dislocation loop and its *actual* size. A human eye is sensitive to *changes* in contrast, and so the absolute contrast level may not be the best criterion for the identification of the 'edge' of a feature visible in an image (in our case, the image of a dislocation loop). To determine the position of the edge of an image we examine all the pixels along the direction parallel to the loop habit plane for edge-on loops and identify the first pixel p where the contrast

relative to background exceeds 15%. Then in the pixels along the direction containing p we check if the change in contrast $(I_p - I_{p-1})/I_{p-1}$ exceeds some threshold value. The process is repeated until a pixel p is found which does satisfy the criteria hence locating one of the edges of the image. A similar procedure is repeated to locate the opposite edge of the image. By subtracting the coordinates of the pixels we determine the maximum image size of edge-on loops. We found that these criteria give good agreement with measurements made by eye for the same simulated image.

Fig. 3 shows values of the image size measured in this way for edge-on Frank loops of various size, imaged under various diffraction conditions and for various foil thicknesses. We see that the image size is a reasonably good measure of the true loop size, with a variation in a range about ±20%. At small loop sizes the images of edge-on Frank loops tend to be a little larger than the true loop size, possibly as a consequence of the way in which we define the edge of a loop image and make the geometrical correction. For loops of size $\geqslant 5$ nm on average there is a reasonably good correspondence between the image size and the true loop size for most foil thicknesses. Similar results were found for other loop orientations [10].

What is the origin of fluctuations of the visible size of small loops? To answer this question we follow the argument by Lewis and Villagrana [12]. The non-parallel propagation of diffracted beams inside the foil results in that every point in an image is a superposition of contributions from waves scattered by various parts of the distortion field of the defect. To give an estimate, we may say that the intensity at the exit surface is a superposition of waves forming the Takagi triangle and converging to a given point at an image from a range of directions defined by the Bragg angle $\theta_B \sim g/k$. For 100 keV electrons and 002 reflection in copper the Bragg angle is $\theta_B \approx 2.0 \times 10^{-2}$ rad. Depending on the depth of the loop in the foil, each point in the image is formed by waves converging from the linear region of size $w \sim \theta_B L$, where L is the distance between the loop and the exit surface. For $L = 60$ nm we find $w \sim 1.2$ nm. Comparing this estimate with the scale of image size fluctuations shown in Fig. 3 we see that it is the non-parallel propagation of diffracted beams first noted by Lewis and Villagrana [12] that is mainly responsible for the uncertainties associated with the identification of the size of small defect clusters. Recently on the basis of multislice image simulations Schäublin [13] came to a similar conclusion that if the size of a defect cluster is smaller than 2 nm, the electron microscope image no longer exhibits the readily identifiable features required, for example, for the determination of the morphology of the defect.

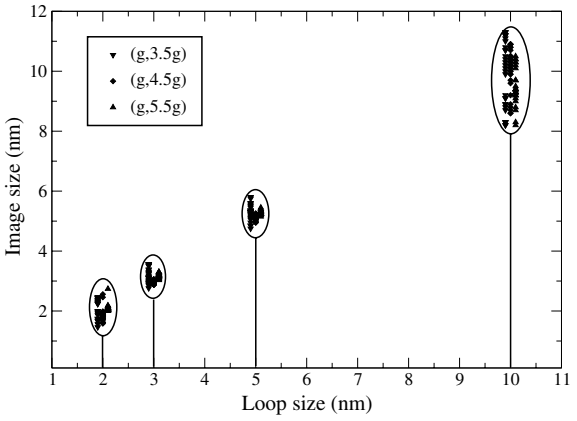

Fig. 3. Image sizes measured by the method described in the text for true loop sizes of 2, 3, 5 and 10 nm. The results presented here are for edge-on Frank loops imaged under the weak-beam conditions for $\mathbf{g} = 002$. The energy of high-energy electrons is 100 keV. Calculations were carried out over a range of foil thickness 54–60 nm in steps of 0.2 nm encompassing one thickness fringe cycle, with each point representing a particular foil thickness (some points are superimposed).

4. Diffuse scattering by small dislocation loops

Diffuse scattering by individual small dislocation loops has recently been extensively investigated using a new experimental technique [6,14] where a nearly parallel beam of electrons is used to illuminate a relatively small area of the foil containing a loop. Whereas in principle the cross-section of diffuse scattering can be evaluated by evaluating the Fourier transform of the amplitudes of diffracted beams found by solving the Howie–Basinski equations (5), a faster method uses either the kinematical approach [15] or the dynamical diffraction approach where electrons scattered by the field of elastic distortions associated with the loop also undergo dynamical diffraction in the foil before and after the actual event of diffuse scattering. The cross-section of *dynamical* diffuse scattering is given by [16]

$$\frac{d\sigma(\mathbf{k}_0 \to \mathbf{k}')}{do} = \left| \int d\mathbf{r} \psi_{-\mathbf{k}'}(\mathbf{r}) \sum_n [V(\mathbf{r} - \mathbf{r}_n - \mathbf{u}_n) - V(\mathbf{r} - \mathbf{r}_n)] \psi_{\mathbf{k}_0}(\mathbf{r}) \right|^2, \quad (7)$$

where $\psi_{\mathbf{k}}(\mathbf{r})$ is a Bloch wave function (1) corresponding to the incident electrons with wave vector $\mathbf{k}$. In the kinematical limit $\psi_{\mathbf{k}}(\mathbf{r}) = \exp(i\mathbf{k}\cdot\mathbf{r})$, and the distribution of intensity given by (7) exhibits features similar to those observed experimentally [6].

We have already noted the significant part played by dynamical diffraction effects in diffraction imaging of dislocation loops. Qualitatively the origin of the strong interference effects seen in Fig. 2 (bottom line) is associated with the fact that the loop is illuminated by a strongly spatially modulated Bloch wave, as opposed to illumination by a weakly distorted plane wave in the case of weak-beam imaging for non-integer values of parameter n. Similarly, we should expect that the distribution of intensity of diffuse scattering is going to be strongly affected by dynamical diffraction effects if the orientation of wave vectors is close to directions for which one or more reciprocal lattice vectors $\mathbf{g}$ satisfy the condition $\mathbf{k}^2 \approx (\mathbf{k}+\mathbf{g})^2$ for either the incident ($\mathbf{k} = \mathbf{k}_0$) or the scattered ($\mathbf{k} = \mathbf{k}'$) electrons.

A comparison between diffuse scattering patterns simulated using the kinematical and dynamical approaches is made in Fig. 4. The general similarities of these patterns suggest that the kinematical approximation is adequate for qualitative studies of diffuse scattering intensity distributions. On the other hand, dynamical effects can still be seen in the diffuse scattering patterns, so a dynamical approach would be necessary for quantitative studies. Comparing the dynamical effects presented in diffraction contrast (Fig. 2) and diffuse scattering (Fig. 4), we see that the effects of dynamical diffraction seem to be less pronounced in diffuse scattering patterns than in diffraction images. The nature of this difference requires further investigation.

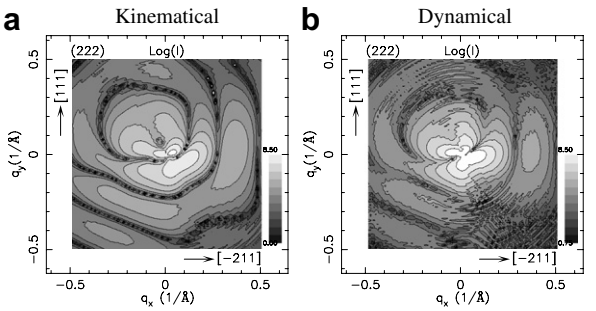

Fig. 4. Iso-intensity plots of elastic diffuse scattering patterns (ignoring Laue scattering) from an vacancy Frank loop of Burgers vector $= 1/3[1\bar{1}1]$ in gold around a (222) Bragg spot under diffraction condition $(\mathbf{g}, 4\mathbf{g})$ where $\mathbf{g} = 111$. (a) Calculated using the kinematical approach, (b) calculated using the dynamical diffraction approach. Intensities are plotted on a common logarithmic scale.

5. Summary

- We implemented a propagation–interpolation algorithm for solving the Howie–Basinski equations, and investigated weak-beam images of three-dimensional defect clusters as a function of the foil thickness, the depth of defect in the foil and diffraction conditions.
- Simulations show that the non-parallel propagation of diffracted beams in the foil introduces significant uncertainty in the interpretation of images of small defects.
- Measurements of elastic diffuse scattering offer an alternative, reciprocal space method of characterizing small loops. Simulations of diffuse scattering patterns exhibit notable dynamical diffraction effects affecting the distribution of intensity in the vicinity of the Bragg diffraction condition.

Acknowledgements

This work performed at UKAEA was funded by the UK Engineering and Physical Sciences Research Council (EPSRC), by the EXTREMAT integrated project under contract number NMP3-CT-2004-500253, and by EURATOM.

References

[1] M.L. Jenkins, M.A. Kirk, Characterisation of Radiation Damage by Transmission Electron Microscopy, Institute of Physics, Bristol, 2001.
[2] M.L. Jenkins, Z. Zhou, S.L. Dudarev, A.P. Sutton, M.A. Kirk, J. Mater. Sci. 41 (2006) 4445.
[3] R. Schäublin, Microsc. Res. Tech. 69 (2005) 305.
[4] A. Howie, Z.S. Basinski, Philos. Mag. 17 (1968) 1039.
[5] Z. Zhou, S.L. Dudarev, M.L. Jenkins, A.P. Sutton, M.A. Kirk, Mater. Sci. Eng. A 400&401 (2005) 80.
[6] M.A. Kirk, R.S. Davidson, M.L. Jenkins, R.D. Twesten, Philos. Mag. 85 (2005) 497.
[7] H. Hashimoto, A. Howie, M.J. Whelan, Proc. R. Soc. London A 269 (1962) 80.
[8] C.J. Humphreys, P.B. Hirsch, Philos. Mag. 18 (1968) 115.
[9] J.M.K. Wiezorek, A.R. Preston, C.J. Humphreys, in: Electron Microscopy and Analysis Group Conference EMAG95, Institute of Physics Conference Series, Ser. 147, Institute of Physics Publishing, Bristol and London, 1995, p. 455.
[10] Z. Zhou, M.L. Jenkins, S.L. Dudarev, A.P. Sutton, M.A. Kirk, Philos. Mag. 86 (2006) 4851.
[11] M.L. Jenkins, M.A. Kirk, H. Fukushima, J. Electron Microsc. 48 (1999) 323.

[12] A.L. Lewis, R.E. Villagrana, Acta Crystallogr. A35 (1979) 276.
[13] R. Schäublin, Selection of experimental methods for JANNUS, presentation on task TW6-TTMS007-D12 given at the 2006 EFDA Monitoring Meeting, CRPP Lausanne, December 2006 (unpublished).
[14] M.A. Kirk, M.L. Jenkins, Z. Zhou, R.D. Twesten, A.P. Sutton, S.L. Dudarev, R.S. Davidson, Philos. Mag. 86 (2006) 4797.
[15] Z. Zhou, A.P. Sutton, S.L. Dudarev, M.L. Jenkins, M.A. Kirk, Proc. R. Soc. London A 461 (2005) 3935.
[16] L.-M. Peng, S.L. Dudarev, M.J. Whelan, High-Energy Electron Diffraction and Microscopy, Oxford University Press, Oxford, 2004, p. 234.